DOI: 10.13009/EUCASS2025-644
11TH EUROPEAN CONFERENCE FOR AERONAUTICS AND SPACE SCIENCES (EUCASS)

Precise orbit prediction for GEO and MEO non-cooperative objects: experimental validation using a passive ground-based optical station

Eliot Stein[1†], *Thomas Delaite*[1*], *Lamberto Dell'Elce*[2], *Hanae Labriji*[1], *Florian Thuillet*[3], *Frédéric Cassaing*[1]
[1]*DTIS, ONERA, Université Paris-Saclay, 91120 Palaiseau, France*
[2]*McTAO, INRIA, Université Côte d'Azur, 06902 Sophia Antipolis, France*
[3]*DTIS, ONERA, Université de Toulouse, 31000 Toulouse, France*
eliot.stein@onera.fr · frederic.cassaing@onera.fr
[*]*At the time of his contribution to this work*
[†]Corresponding author

Abstract

Enhanced tracking of resident space objects (RSOs) plays a key role in improving the safety and sustainability of space operations. However, the accuracy of observations constrains the orbit determination (OD) of RSOs. Passive ground-based optical stations, which serve as a convenient source of sensing devices for medium- and high-Earth-orbits (MHOs), provide angular measurements with typical accuracies ranging from 150 to several hundred milliarcseconds (mas). Following successive nights of observations, an RSO's orbit can be determined with an accuracy of a few hundred meters. The CICLOPE station, which was recently developed at ONERA, provides data with 50 mas angular accuracy. This corresponds to an accuracy of 5–10 m at MHO distance, which is sufficient to detect deviations from well-known gravitational dynamics over a few hours, such as those due to solar radiation pressure (SRP).

This paper demonstrates what we call precise orbit prediction (POP), which achieves decametric accuracy over two days for non-cooperative MHO RSOs using angle-only measurements. In practice, we first determine which contributors are needed to model forces with sufficient accuracy and then build the propagator accordingly. Based on the constructed force model, we develop a precise orbit determination (POD) algorithm using a weighted least squares method and a Jacobian derived from variational equations. After validating the algorithm, we evaluate the POP performance using observations derived from precise ephemerides of reference satellites. We add a characteristic 50 mas random noise to simulate experimental angle measurements overnight with a low acquisition frequency. Initially, using only standard gravitational models, we obtain hectometric errors on propagated orbits, which underscores the importance of NGP residuals. Adding next-night observations to estimate SRP parameters accurately yields an accuracy of 14 m over the POD time span, increasing to 30 m over the 48-hour POP period. Finally, we demonstrate the decametric accuracy of our POP solution using CICLOPE data.

1. Introduction

Medium Earth Orbit (MEO) and Geostationary Earth Orbit (GEO) play a critical role in positioning, Earth observation, telecommunications, and defense. Consequently, the early identification and characterization of satellite proximity events is of paramount importance for space-faring nations. However, the increasing reliance on satellite-based services has resulted in increased congestion in these orbital regions[10]. This phenomenon is particularly evident in GEO, where the proliferation of resident space objects (RSOs) poses significant long-term sustainability challenges. While the spacing of satellites along the GEO arc remains relatively wide, the necessity of maintaining reliable debris tracking and mitigating potential collision hazards is increasing. Space Situational Awareness (SSA) is defined as the detection, tracking, and characterization of RSOs in the near-Earth environment, ensuring long-term sustainability and safe access to space. For collision avoidance, as well as for optimizing satellite operations and managing space traffic effectively, accurate orbit predictions are essential.

When observing objects in medium- and high-Earth orbits (MHO), passive ground-based optical stations (PGBOS) remain the primary source of data. However, these sensors present two main limitations. First, their operation is restricted to cloud-free, nighttime conditions. Second, they provide angle-only measurements, with typical accuracy traditionally ranging from a few hundred milliarcseconds (mas)[29,35] to approximately 150 mas[15,27]. Following successive nights of observation, the orbit of a resident space object (RSO) can be determined with an accuracy of a few hundred meters[20]. More advanced Satellite Laser Ranging (SLR) stations enable millimetric accuracy on cooperative RSOs equipped with optical retro-reflectors, such as Global Navigation Satellite System (GNSS) satellites. However, the use of SLR on non-cooperative RSOs is generally limited to LEO, with resulting positional accuracies ranging from decameters to hectometers[6,24,25].

Improving accuracy on distant non-cooperative RSO generally requires larger telescopes for the collection of a greater number of photons, generally at the expense of field and cost. Leveraging the latest hardware and algorithmic advances, the recently developed the CICLOPE station at ONERA, which achieves an angular accuracy of 50 mas while remaining lightweight, cost-effective, and easily deployable on a large scale. This enhanced observational performance facilitates the precise orbit determination (POD) of non-cooperative RSOs through a better inference of dynamical parameters associated with fine dynamical models. Once the object's state has been adequately characterized, a reliable precise orbit prediction (POP) can be performed. The objective is to achieve decametric accuracy over 48 hours. However, given the inherent non-linearity of the POD problem, it is imperative to achieve precise modeling of the dynamical environment and robust estimation of the object's state.

In this work, we propose and demonstrate a method for the POD and POP of non-cooperative MHO RSOs. Section 2 first shows that recent advances enable the accurate measurement of RSO position (upper bloc of Fig. 1) with an accuracy of 50 mas. Then, in Sec. 3, we show that Direct Solar Radiation Acceleration (DSRA) is the main unknown contributor in the motion model, thus we derive a simplified dynamical model to account for its effects, as well as define an estimation method for the RSO's state, leading to a POD algorithm (lower bloc). Lastly, in Sec. 4, we show with various data from experimental measurements (online ephemerides or data collected with our PGBOS CICLOPE) that this simplified model accurately fits the finest RSO's orbit, enabling the prediction of a non-cooperative RSO's position with decametric accuracy over several days.

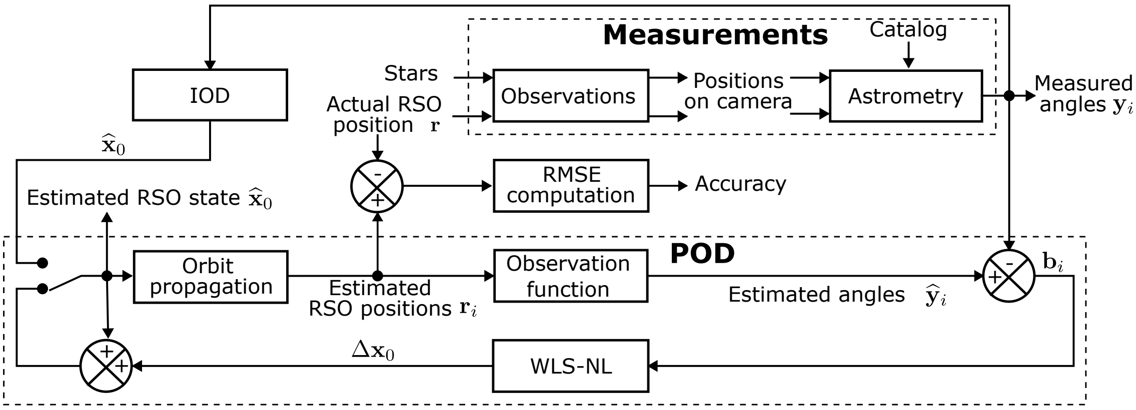

Figure 1: Schematic dataflow.

2. Fine optical measurement of RSO position and observability of dynamical effects

The domain of space surveillance with optical telescopes has undergone profound changes in recent years. The advent of SSA, in conjunction with the burgeoning fields of transient astronomy[5] and high-end amateur astronomy[1], has precipitated the availability of fast wide-field optical tubes and robotic components, which are now readily available at a moderate cost. Concurrently, large sCMOS detectors operate close to the quantum limit, exhibiting high sensitivity and extremely low noise, and offer high frame rates, as required by the observation of moving objects. Furthermore, the advent of rapid, cost-effective GPU technology has paved the way for the real-time processing of data streams. Finally, the publication of precise astrometric catalogues[11], derived from fine measurements conducted by dedicated satellites, enables the estimation and correction of atmospheric refraction, accounting for its spatial and chromatic variations[34].

2.1 Demonstrated accuracy on position measurements

These advances have led to position measurements of 'fast-moving' (for astronomers, with an apparent velocity lower than 2 "/s) Near-Earth Objects from the ground, using a stack of a hundred of 1 s exposure images on a metric reflective telescope, with an accuracy better than 10 mas[34]. For an SSA survey telescope, objects in Earth orbit have a much higher apparent speed (45 "/s for GNSS satellites) while limited integration times are required to scan the full sky. In addition, RSO measurements are expected in the GCRS reference frame, whereas astrometric catalogs are in the ICRS, and refraction correction is performed in elevation. Furthermore, contributions specific to SSA, such as the parallax angle induced by the proximity of the RSO[13] have to be considered. All these adjustments can be performed in a dedicated observation function (Fig. 1).

To evaluate the interest of these new technologies for SSA, Onera has built CICLOPE, a passive ground-based optical station[8], now located at the Salon-de-Provence Air Base, based on a RASA14 tube with a 6Kx6K sCMOS camera leading to a pixel scale of 2600 mas. Its performance has been computed by comparing the estimated position of reference GNSS satellites with their accurately known and published ephemerides. We demonstrated a 2D astrometric accuracy of 50 mas (Fig. 2) using only 10 s measurements[7], corresponding to 5 m (resp. 10 m) in MEO (resp. GEO) orbits, *i. e.* the accuracy of the measurement is comparable to the typical size of these satellites, which is a significant feature for collision avoidance. This also shows that a 36 cm-diameter telescope made of commercial components can produce results around one order of magnitude better than what is usually available.

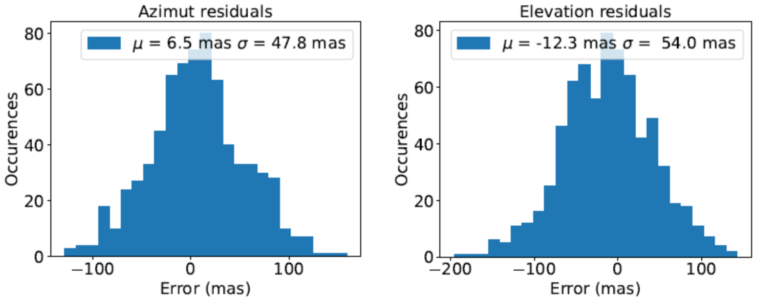

Figure 2: Demonstrated astrometric accuracy of CICLOPE, measured on Galileo 20, 5 to 6 Aug 24, 23h–2h30, with elevation angles varying between 48°, up to 75° and down to 63°.

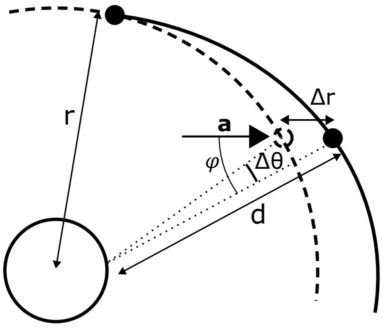

Figure 3: Apparent shift $\Delta\theta$ as a function of the angle φ of **a**.

2.2 Observability of DSRA-Induced Dynamical Effects

Passive optical measurements only provide two projections, perpendicular to the line of sight, of the RSO position and possibly its velocity. The radial components are lost. The next step is thus to collect several dated position estimates along the trajectory of the observed RSOs, to compute their orbital parameters and derive their future position. Once an orbital model is identified (see Sec. 3), accurate position measurements can be used to finely tune the RSO's estimated state.

If a very small constant acceleration $\delta\mathbf{a}$ is added to a perfectly known orbit and integrated during a small duration Δt, the departure from the expected position is (at first order, for a very small shift $\Delta\mathbf{r}$)[31]:

$$\Delta\mathbf{r} = \frac{1}{2}\,\delta\mathbf{a}\,\Delta t^2. \tag{1}$$

The apparent effect $\Delta\theta$, for an observer on the ground at a distance d, is maximum when the angle φ between **a** and the line of sight is $\pi/2$ and null when $\varphi = 0$ (Fig. 3). More precisely:

$$\tan\Delta\theta = \frac{|\Delta\mathbf{r}|}{d}\sin\varphi. \tag{2}$$

Thus, for a small angle $\Delta\theta$, taking a generic average value $\sin\varphi \approx 0.5$ (as φ changes during the arc because of the RSO and observer motions) and assuming that $d \approx r$ for high Earth orbits, an order of magnitude of the typical acceleration amplitude $\widehat{\delta a}$ that can be estimated is:

$$\widehat{\delta a} \approx r\left(4\,\frac{\Delta\theta}{\Delta t^2}\right). \tag{3}$$

Using CICLOPE's value $\Delta\theta = 50$ mas from Sec. 2.1 and a typical nightspan $\Delta t \approx 6$ h, we find (in SI units) $\widehat{\delta a}/r \approx 2.1\;10^{-15}$. The capacity to detect and measure such small accelerations enables the Precise Orbit Determination performed in next section.

DOI: 10.13009/EUCASS2025-644

3. An efficient model for orbit determination and prediction

3.1 Precise dynamics modeling

To generate the orbit of an RSO, one must first model the dynamics of the system. The solution $\mathbf{x}(t)$, which typically includes position, velocity, and possibly additional dynamical parameters, evolves according to the ordinary differential equation (ODE):

$$\dot{\mathbf{x}} = f(\mathbf{x}, t), \tag{4}$$

where f is the vector field representing the system dynamics. Provided that f satisfies the Cauchy–Lipschitz conditions (namely, that it is Lipschitz-continuous in $\mathbf{x}$ and continuous in t), the ODE admits a locally unique solution for any given initial state. Let $\mathbf{x}_0 = \mathbf{x}(t_0)$ be the reference state (or initial state) at a reference epoch t_0. Then, the flow ϕ^t is defined[17] as the smooth function associated with the vector field f, assigning to any initial condition $\mathbf{x}_0$ the unique solution $\mathbf{x}(t)$, such that:

$$\mathbf{x}(t) = \phi^t(\mathbf{x}_0). \tag{5}$$

Achieving decametric-level accuracy in predicting the position of an RSO requires careful modeling of the perturbing accelerations included in f. However, as additional force models are introduced, solving equation (5) analytically becomes increasingly impractical. Consequently, a standard approach is to numerically integrate equation (4), starting from a well-chosen initial state (as described in Sec. 3.3.1), while selecting the appropriate dynamical effects to include. For this classical topic, we have used the models listed in Tab. 1. All are deterministic, except for the solar radiation pressure (SRP) which depends on parameters that may not be known. Section 3.2 will show that all the Direct Solar Radiative Acceleration (DSRA) parameters can be gathered in a single acceleration called the a_{IAM}, and whose typical values are listed in Tab. 2.

Table 1: Summary of the orbit propagation strategy.

	Model
Geopotential	EGM2008 (tide-free)[21]
Third-body	Moon and Sun (analytical position model[32])
Solar radiation pressure	Isotropic absorbance and spherical RSO[32]
Earth shadow	Conical model where the eclipsing factor scales with the Sun's visible area[18]
Transformations	Topocentric (AltAz), GCRS (Cartesian), ICRS (RADec) via Astropy[2–4]
Integration method	Explicit Runge-Kutta method of order 5(4)[9] with quartic interpolation of the solution[28] via Scipy[33]

Table 2: Typical DSRA dynamical parameters, as defined in Eq. (9), for various types of RSOs.

RSO type	typ. area (m^2)	typ. mass	typ. $c_R A_{\mathrm{eq}}/m$ ($\mathrm{m}^2\,\mathrm{kg}^{-1}$)	typ. a_{IAM} $\mathrm{nm\,s}^{-2}$
Telecommunication (GEO)	tens	2 to 6 t	0.01 to 0.05	45 to 230
GNSS	moderate	0.7 to 2 t	0.02 to 0.08	90 to 360
Earth Observation	large	0.5 to 3 t	0.03 to 0.1	130 to 450
CubeSats, small sats	typically < 1	1 to 10 kg	1	
Large Debris	tens	1-10 t	0.01 to 0.05	45 to 230
Small Debris	very small	few g to a few kg	0.1 to 10	450 to 45 000
Solar sails	very large	< 100 kg	> 10	> 45 000

The main issue is to select terms to be considered or neglected in the vector field f, to trade-off accuracy and computing time. This can be done with the help of Fig. 4, which plots the acceleration induced by some contributors as a function of the distance to the Earth's center. The typical accuracy of a ground-based station, based on Eq. (3), and values of Tab. 2, are included. It shows that the DSRA, although varying a lot depending on the type of RSO, is of the order of $10^{-7}\,\mathrm{m\,s}^{-2}$. This can induce relative position shifts of hundreds of meters over an orbital revolution at high altitudes[19]. Our objective is to reach a decametric error over a 24 to 48 h period, therefore the main focus of this work will be to model SRP in a reliable fashion. The main output of this plot is that the new possibility of accurate positioning from the ground unlocks the possibility to reliably infer DSRA dynamical parameters (assuming they are

DOI: 10.13009/EUCASS2025-644

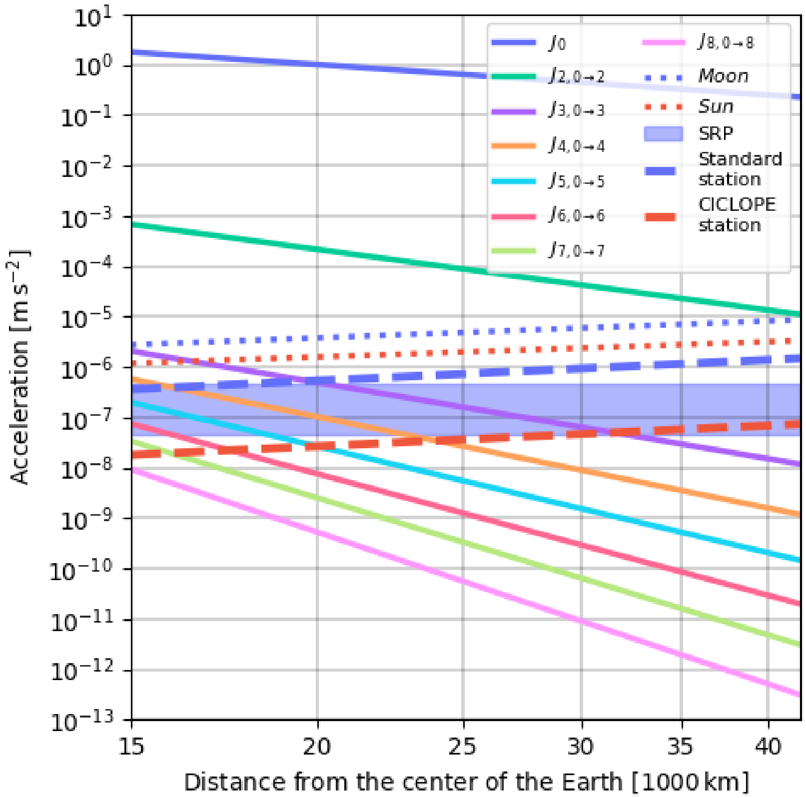

Figure 4: Perturbation magnitude as a function of the distance to Earth's center of mass, inspired from[18]. The vertical axis expresses the acceleration associated with each force. Quantities are integrated over latitude and longitude for both geopotential and 3rd body interactions, and are summed over degrees for the geopotential. The DSRA band values are computed from Tab. 2, excluding values higher than 360 m s^{-2}. The CICLOPE and standard station values are computed taking an angular accuracy of 50 mas and 1 arcsec respectively, and a period of 6 h in Eq. (3).

piece-wise constant) with limited observations, thus enabling accurate orbit propagation over several days. We also see that the modeling of the geopotential up to the 5th order is of the same order of magnitude as that of SRP for low MEO RSOs. At GNSS altitude, propagation accounting for additional 6th, 7th and 8th order contributions yield, at most, a sub-meter improvement in accuracy over 24 h. Since these higher-order terms are handled using the same numerical method as lower-order harmonics, and incur minimal additional computational cost, they are retained in the model. However, smaller contributions on the order of 10^{-8} or smaller (*e.g.*, dynamic solid tides, indirect solar radiation pressure due to Earth's albedo, Earth thermal emission, relativistic corrections, and third-body perturbations from Venus or Jupiter[18]) are neglected, as their overall impact remains negligible.

3.2 Isotropic absorbance model

Solar radiation pressure generates directional forces upon an RSO's exposed surfaces as a result of the momentum transfer of photons radiated by the Sun[19]. In the absence of *a priori* knowledge on the RSO structure and attitude control, the dynamical parameters (RSO's panels' area, orientation, and optical property) estimation problem is severely ill-posed and may lead to degenerate or non-unique solutions. By assuming a uniform spherical shape, we reduce the dimensions of the parameter space, thereby simplifying its exploration. Sun radiation strikes the ball symmetrically, canceling all momentum transfers that are not along the sun axis $\mathbf{e}_{\odot}$. We can model an equivalent flat surface of area A_{eq}, with a surface normal $\mathbf{e}_n$ pointing toward the Sun *i.e.* $\mathbf{e}_n = \mathbf{e}_{\odot}$. To account for the optical properties of the exposed area A_{eq}, let us introduce the reflectivity coefficient c_R. While its value can take any continuous value in between, there are three distinct reference cases: 0 (translucent: no momentum transfer), 1 (fully absorptive), and 2 (fully reflective).

In Einstein's special relativity, the energy–momentum relation links the energy E of any particle to its rest mass m_0 and momentum $\mathcal{P}$:

$$E^2 = (\mathcal{P}c)^2 + (m_0c^2)^2, \tag{6}$$

DOI: 10.13009/EUCASS2025-644

where c is the speed of light in a vacuum. For a photon, which is massless, this relation reduces to:

$$\mathcal{P} = \frac{E}{c}. \tag{7}$$

Furthermore, we can write the differential energy of all photons incident on the RSO surface A_{eq} over the considered time span $\mathrm{d}t$ as:

$$\mathrm{d}E_{\mathrm{tot}} = c_R\, A_{\mathrm{eq}}\, \mathcal{F}_\odot\, \mathrm{d}t, \tag{8}$$

where $\mathcal{F}_\odot$ is the solar radiation flux density in the vicinity of Earth in $\mathrm{W\,m^{-2}}$. This is given by $\mathcal{F}_\odot(r_\odot) = \mathcal{F}_{\mathrm{AU}}\,(\mathrm{AU}/r_\odot)^2$ with $\mathcal{F}_{\mathrm{AU}} = 1361\,\mathrm{W\,m^{-2}}$ the mean solar radiation flux density at 1 AU and $r_\odot$ the Earth-Sun distance. Thus, we obtain a simple isotropic absorbance model (IAM) yielding a DSRA in the anti-Sun direction:

$$\ddot{\mathbf{r}}_{\mathrm{IAM}} = -\frac{\mathrm{d}\mathcal{P}/\mathrm{d}t}{m}\mathbf{e}_\odot = -\frac{\mathcal{F}_\odot}{c}\frac{c_R A_{\mathrm{eq}}}{m}\,\mathbf{e}_\odot = -a_{\mathrm{IAM}}\,\mathbf{e}_\odot. \tag{9}$$

In addition to the classical area to mass ratio A_{eq}/m, Eq. (9) shows that c_R and $\mathcal{F}_\odot$ are also involved. The optical properties of an RSO's surface generally are unknown and can vary over time due to aging or surface degradation, while the solar density flux fluctuates with the Sun-Earth distance or solar activity. However, during a few hours to a few days time window, we can consider those values as constants, or only take the average value into account; thus, we will use the global product $a_{\mathrm{IAM}} = \mathcal{F}_\odot c_R A_{\mathrm{eq}}/(mc)$ as the dynamical parameter of the isotropic SRP, which is estimated during the POD and has the dimension of an acceleration.

3.3 Precise estimation

3.3.1 Non linear least square problem

Let h be the observation function which numerically accounts for light propagation, detection, and astrometric data processing (Fig. 1). To estimate RSOs' states and dynamical parameters, according to Eq. (5), we define pure theoretical observations such that:

$$\mathbf{y}(t) = h(t, \mathbf{x}(t)) = h(t, \phi^t(\mathbf{x}_0)) = g(t, \mathbf{x}_0), \tag{10}$$

where g is the initial-state-to-observation function. As this latter equation links an observation $\mathbf{y}(t)$ at any instant t to just one state at a given time t_0, the estimation problem reduces to finding that single state $\mathbf{x}_0$. Therefore, the optimal solution is obtained by jointly minimizing the residuals from all observations, where each residual at observation time t_i is given by:

$$\mathbf{b}_i = \tilde{\mathbf{y}}_i - g(t_i, \mathbf{x}_0), \tag{11}$$

where $\tilde{\mathbf{y}}_i$ denotes the i^{th} observation of the RSO, corrupted by measurement noise. The least squares (LS) problem thus consists in minimizing the quadratic cost function J defined as:

$$J(\mathbf{x}_0) = \sum_{i=0}^{N} \mathbf{b}_i^T W_i \mathbf{b}_i, \tag{12}$$

where N is the total number of observations and W_i is the weight matrix associated to each observation (*i.e.*, the inverse of the observation covariance matrix). However, we cannot directly find the global minimum of J since g is highly non-linear. A first-order linearization around a current estimate $\hat{\mathbf{x}}_0$ enables the use of local iterative methods to converge towards a local minimum. Let us define the initial-state-to-observation matrix (ISOM) as:

$$A(t) = \frac{\partial g(t, \mathbf{x}_0)}{\partial \mathbf{x}_0}. \tag{13}$$

Then, g can be approximated as:

$$g(t, \mathbf{x}_0) \approx g(t, \hat{\mathbf{x}}_0) + A(t)\,(\mathbf{x}_0 - \hat{\mathbf{x}}_0), \tag{14}$$

where $A(t)$ is evaluated at $\mathbf{x}_0 = \hat{\mathbf{x}}_0$. This approach does not guarantee a global optimum, but it provides an effective approximation when initialized close to the true solution. Then, we transform this non-linear problem into a differential correction one by introducing the new variable $\Delta\mathbf{x}_0 = \mathbf{x}_0 - \hat{\mathbf{x}}_0$, defining the residual at time t_i as $\hat{\mathbf{b}}_i = \tilde{\mathbf{y}}_i - g(t_i, \hat{\mathbf{x}}_0)$, and denoting the ISOM at time t_i by $A_i = A(t_i)$, yielding:

$$J(\Delta\mathbf{x}_0) \approx \sum_{i=0}^{N} \left[\left(\hat{\mathbf{b}}_i - A_i\Delta\mathbf{x}_0\right)^T W_i \left(\hat{\mathbf{b}}_i - A_i\Delta\mathbf{x}_0\right)\right]. \tag{15}$$

DOI: 10.13009/EUCASS2025-644

This new formulation allows to express the cost J as a function of the deviation to its minimum, which can be found posing:

$$\nabla_{\mathbf{x}} J(\Delta\mathbf{x}_0) = 0. \tag{16}$$

Solving for $\Delta\mathbf{x}_0$ gives:

$$\Delta\mathbf{x}_0 = \sum_{i=0}^{N} (A_i^T W_i A_i)^{-1} A_i^T W_i \hat{\mathbf{b}}_i, \tag{17}$$

where $(A_i^T W_i A_i)$ is referred to as the normal matrix and the covariance matrix of the estimate is given by the sum $\sum_{i=0}^{N} \left(A_i^T W_i A_i\right)^{-1}$. The inversion is done using a truncated SVD approach that regularizes the inversion by discarding small singular values. The truncation threshold is based on an adaptive criterion that controls the cumulative mean square amplification of the inverted singular values[22]. It prevents the inclusion of components that would disproportionately amplify numerical noise due to small singular values, thus improving numerical stability and mitigating the effects of ill-conditioning.

Starting from an initial guess for the estimate $\hat{\mathbf{x}}_0$, the solution of the OD problem can be found by iteratively incrementing $\hat{\mathbf{x}}_0$ by $\Delta\mathbf{x}_0$, up until a stopping criterion is met (based on the convergence of the cost function J, eventually of its divergence, or the reach of a maximum number of iterations). The choice of the initial guess in the LS process is crucial for highly nonlinear problems, as a poor initialization may lead to convergence toward a local minimum. Therefore, the initial estimate should be as close as possible to the true solution $\mathbf{x}_0$. In practice, it is generally initialized using Gooding's method[12].

3.3.2 State transition matrix and variational equations

As shown in Sec. 3.3.1, the LS process requires to compute the ISOM. We will make use of a classical numerical method to compute the Jacobian through joint numerical integration of differential equations[18,30,32]. We can define the state transition matrix (STM) as the partial derivative matrix of the flow ϕ such that:

$$\Phi(t) = \frac{\partial \phi^t(\mathbf{x}_0)}{\partial \mathbf{x}_0}. \tag{18}$$

Similarly, the observation matrix (OM) can be written as:

$$H(t) = \frac{\partial h(t, \mathbf{x}(t))}{\partial \mathbf{x}(t)}. \tag{19}$$

Starting from Eq. (13) and following the chain rule, we can then define the ISOM as:

$$A(t) = \frac{\partial h(t, \phi^t(\mathbf{x}_0))}{\partial \mathbf{x}_0} = \frac{\partial h(t, \mathbf{x}(t))}{\partial \mathbf{x}(t)} \cdot \frac{\partial \phi^t(\mathbf{x}_0)}{\partial \mathbf{x}_0} = H(t) \cdot \Phi(t). \tag{20}$$

On one hand, H can be computed using finite differences, by setting a differential step ϵ for numerical differentiation. This step is chosen to be of the same order of magnitude as the positioning accuracy of the CICLOPE station. Given that the measurement function can be considered linear at such small angular scales (tens of mas), this approach yields reliable results with minimal computational effort. On the other hand, applying this finite-difference approach for the STM requires multiple orbit propagations: one for the reference trajectory and one for each component of the initial state vector $\mathbf{x}_0$. This can become computationally expensive when spanning several days of observations. Moreover, setting the appropriate differential step is a delicate task, as its value strongly influences the accuracy of the computed derivatives over long periods and in the presence of chaotic gravitational dynamics. Therefore, the STM is numerically integrated alongside $\mathbf{x}(t)$. Let us derive its ODE. From equations (4) and (5), we have:

$$\frac{\mathrm{d}}{\mathrm{d}t}\left(\phi^t(\mathbf{x}_0)\right) = \dot{\mathbf{x}} = f(\phi^t(\mathbf{x}_0)). \tag{21}$$

Since the flow ϕ^t is smooth, we have:

$$\dot{\Phi}(t) = \frac{\mathrm{d}}{\mathrm{d}t}\left(\frac{\partial \phi^t(\mathbf{x}_0)}{\partial \mathbf{x}_0}\right) = \frac{\partial}{\partial \mathbf{x}_0}\left(\frac{\mathrm{d}\phi^t(\mathbf{x}_0)}{\mathrm{d}t}\right) = \frac{\partial}{\partial \mathbf{x}_0}\left(f(\phi^t(\mathbf{x}_0))\right). \tag{22}$$

Using the chain rule, we obtain:

$$\dot{\Phi}(t) = \frac{\partial f(\mathbf{x})}{\partial \mathbf{x}} \cdot \frac{\partial \phi^t(\mathbf{x}_0)}{\partial \mathbf{x}_0} = \nabla_{\mathbf{x}} f(\mathbf{x}) \cdot \Phi(t). \tag{23}$$

DOI: 10.13009/EUCASS2025-644

In our dynamical models, the time derivative of position (*i.e.* the velocity) does not explicitly depend on the position nor the dynamical parameters, consequently, it is straightforward to compute. By contrast, the time derivative of velocity (*i.e.*, the acceleration) depends explicitly on both and thus requires a more involved processing. The derivations for gravitational models are well documented in the literature[18,30,32]. Let us derive the variational equations of the IAM.

3.3.3 Partial derivatives of the isotropic absorbance model

Let us begin with the partial derivative with regard to position. According to Eq. (9), we get:

$$\frac{\partial \ddot{\mathbf{r}}_{\mathrm{ISO}}}{\partial \mathbf{r}} = -a_{\mathrm{IAM}} \frac{\partial \mathbf{e}_{\odot}}{\partial \mathbf{r}}. \tag{24}$$

Note that we consider a_{IAM} to be piece-wise constant, yielding $\partial a_{\mathrm{IAM}}/\partial \mathbf{r} = \mathbf{0}_3^T$ for the period of the POD (and POP). We recall that the derivative of the unit vector $\mathbf{e}_u$ derived from any vector $\mathbf{u}$ is given by:

$$\frac{\partial \mathbf{e}_u}{\partial \mathbf{r}} = \frac{1}{|\mathbf{u}|} \left(\mathbf{I}_3 - \mathbf{e}_u \mathbf{e}_u^T \right) \frac{\partial \mathbf{u}}{\partial \mathbf{r}}, \tag{25}$$

where $\mathbf{e}_u \mathbf{e}_u^T$ denotes an outer product. Thus, it yields:

$$\frac{\partial \ddot{\mathbf{r}}_{\mathrm{ISO}}}{\partial \mathbf{r}} = -a_{\mathrm{IAM}} \frac{1}{|\mathbf{r}_{\odot}|} \left(\mathbf{I}_3 - \mathbf{e}_{\odot} \mathbf{e}_{\odot}^T \right). \tag{26}$$

The partial derivative with regard to the dynamical parameter is trivial:

$$\frac{\partial \ddot{\mathbf{r}}_{\mathrm{ISO}}}{\partial a_{\mathrm{IAM}}} = -\mathbf{e}_{\odot}. \tag{27}$$

With these equations, we are now able to compute $\nabla_{\mathbf{x}} f(\mathbf{x})$ and thus to integrate the ODE of Φ from Eq. (23) alongside that of $\mathbf{x}$ in Eq. (4). The STM values are evaluated at the time of each observation, together with the value of the OM, allowing the computation of the ISOM for each observation and thus the minimization of the J criterion.

4. Results

This section reports our results, obtained first with simulated satellites (Sec. 4.2), then with actual precise measurements on reference satellites (introduced in Sec. 4.1) purposely degraded to simulate the accuracy of a PGBOS (Sec. 4.3), and last with actual optical data obtained with our station CICLOPE (Sec. 4.4). To quantify the quality of our solutions, we introduce the absolute error on position and velocity at time t_i as in Eq. (28), where $\mathbf{r}^{\mathrm{ref}}$ and $\mathbf{v}^{\mathrm{ref}}$ respectively are the position and velocity of our reference state (generally the on-line precise ephemerides defined in Sec. 4.1), and $\mathbf{r}^{\mathrm{sol}}$ and $\mathbf{v}^{\mathrm{sol}}$ are those of our solution. We also define the relative error as in Eq. (29), which allows us to compare different quantities as it is dimensionless.

$$\mathrm{AE}r_i = \left| \mathbf{r}_i^{\mathrm{sol}} - \mathbf{r}_i^{\mathrm{ref}} \right|, \qquad \mathrm{AE}v_i = \left| \mathbf{v}_i^{\mathrm{sol}} - \mathbf{v}_i^{\mathrm{ref}} \right|, \tag{28}$$

$$\mathrm{RE}r_i = \frac{\left| \mathbf{r}_i^{\mathrm{sol}} - \mathbf{r}_i^{\mathrm{ref}} \right|}{\left| \mathbf{r}_i^{\mathrm{ref}} \right|}, \qquad \mathrm{RE}v_i = \frac{\left| \mathbf{v}_i^{\mathrm{sol}} - \mathbf{v}_i^{\mathrm{ref}} \right|}{\left| \mathbf{v}_i^{\mathrm{ref}} \right|}. \tag{29}$$

These errors are defined for a unique state, thus, to compare whole trajectories, we use Eq. (28) to define the root mean square of the absolute position error:

$$\mathrm{RMSE}r = \sqrt{\frac{1}{n} \sum_{i=1}^{n} (\mathrm{AE}r_i)^2}. \tag{30}$$

4.1 Reference data

In order to evaluate the quality of the dynamic models and the estimator, we rely on ESA's GNSS ephemerides, accurate to the centimeter level and publicly available* with a sampling period of 300 s. We use the June 2024 MGNSS final products, near the summer solstice to avoid the eclipse season. In the following, these data are considered as ground truth ($\mathbf{r}_i^{\mathrm{ref}}$ in Eqs (28-29)), and observations as well as errors are derived from these ephemerides.

---

*http://navigation-office.esa.int/products/gnss-products/

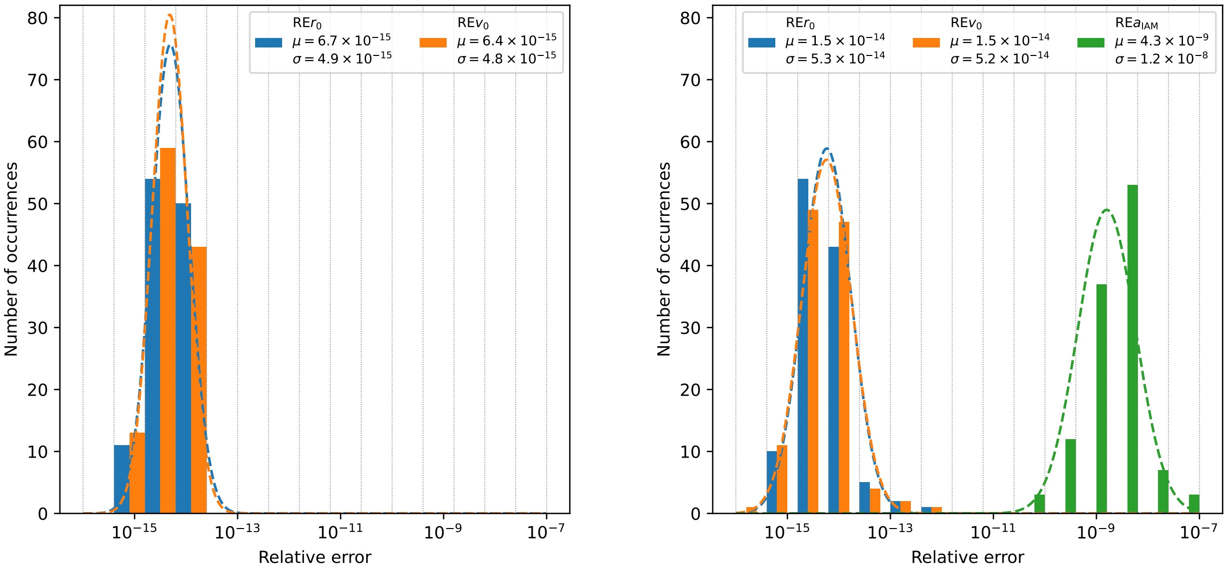

(a) Gravitational models only. **(b)** Isotropic absorbance included.

Figure 5: Histogram of the error of initial guess parameters for 116 RSOs. Vertical grey lines show the binning.

4.2 Technical validation by simulation

The first point in our study is a technical validation of the estimator, using the so-called inverse crime. Each initial state of the 116 various RSOs from the reference data is propagated over one entire revolution. We then sample the position and velocity of the RSO on this propagated orbit every 5 min, which we directly use as 6D observations. Finally, we generate an initial guess for our estimator from a normal law centered around the true initial state, with a standard deviation of 25 m and 0.025 m s^{-1} for each axis of position and velocity respectively. Using the same propagator as for generating the reference orbit, the 6D observations derived from it, and the described initial guess, the POD process should then return the true state of the satellite, within a numerical error range. Fig. 5(a) shows a histogram of the relative position and velocity error REr_0 and REv_0 for the reference initial epoch across all PODs, when modeling solely the gravitational dynamics. Under those conditions, PODs lead to an average REr_0 and REv_0 of the order of 10^{-15}. Values of standard deviation are within the same range, indicating consistency in the PODs. This corresponds to the numerical accuracy level and has no noticeable effect on the accuracy of a POP. Although these test results are not shown here, they confirm that the influence is negligible.

Let us now determine orbits with the IAM included in the dynamics. To increase the diversity of the reference orbits, we generate a randomly selected a_{IAM} within the range described in Tab. 2, while the initial guess for the POD was set to $a_{\mathrm{IAM}} = 90\,\mathrm{nm\,s^{-2}}$ as it is a reasonable value for most MHO RSOs (such as telecommunication, GNSS, weather satellites or large debris). Fig. 5(b) illustrates the same quantities as Fig. 5(a), along with the relative error of the DSRA dynamical parameter REa_{IAM}. We notice that the mean REr_0 and REv_0 are doubled as compared to Fig. 5(a), while their standard deviation is an order of magnitude higher. This is still extremely small, however we see that adding a dynamical parameter to estimate has the effect of slightly decreasing the consistency of the POD, under identical measurement conditions. The least accurately estimated parameter is a_{IAM}, with an average relative error of 10^{-9} and a standard deviation one order of magnitude higher. However, such an error would correspond to a perturbation of only $10^{-16}\mathrm{m\,s^{-2}}$ on Fig. 4, and is therefore still negligible in practice. Overall, the algorithm successfully retrieved the original parameter in a few number of iterations.

4.3 Validation in a realistic case with simulated optical data

The next step consists of validating the complete POD pipeline, including both the dynamical modeling and the estimation procedure, in realistic observational scenarios. Based on the full reference ephemerides, we generate angle-only observations adding a pseudo-random gaussian noise with a variance similar to CICLOPE measurements. In this section, the observer is located at a fixed location, and therefore, only a subset of 17 GPS satellites can be consistently observed over five consecutive nights for more than 1 h (at a rate of 3 observations per hour), due to their orbital period

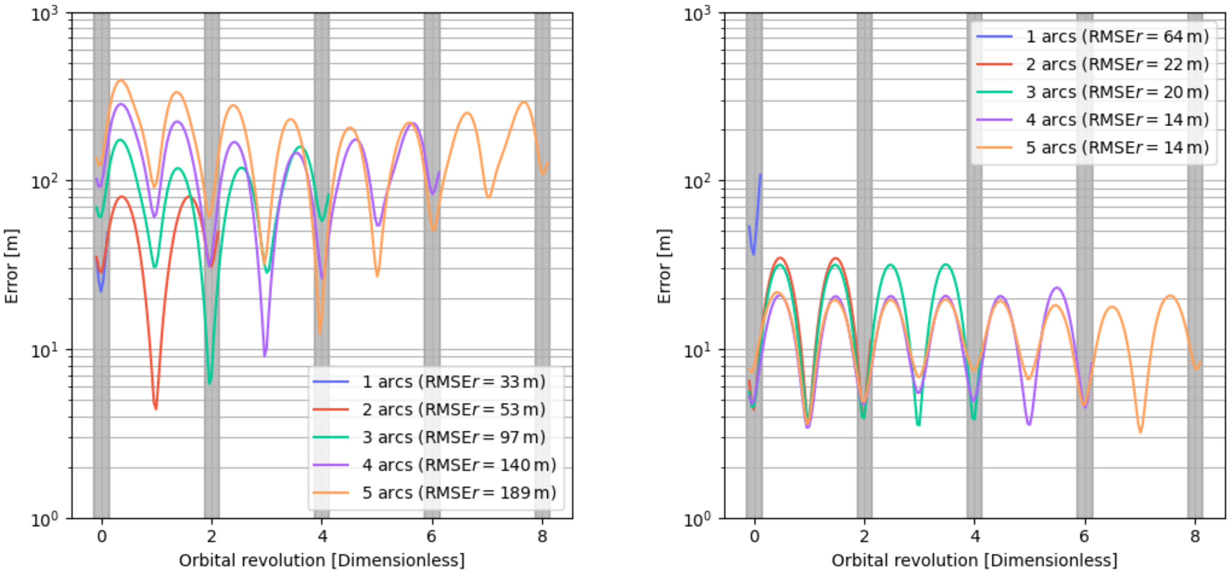

(a) Gravitational models only.

(b) Isotropic absorbance included.

Figure 6: AEr during the period of the POD. POD solutions for different numbers of observation arcs are represented. Each curve is the average value of the 17 GPS satellite solutions. Grey bands represent the average observation arc period.

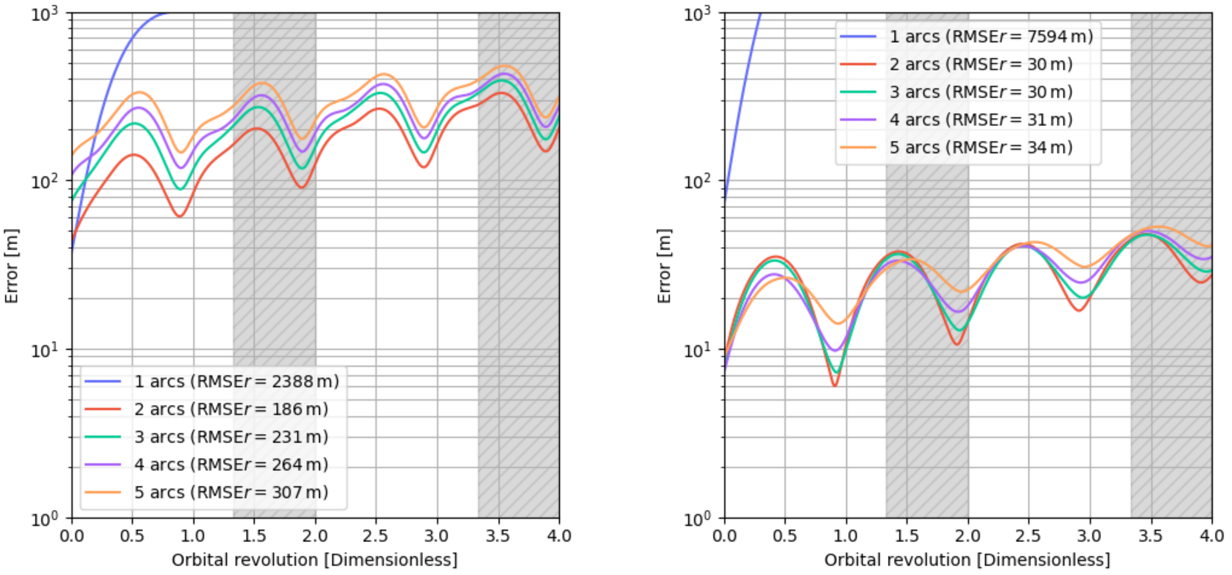

(a) Gravitational models only.

(b) Isotropic absorbance included.

Figure 7: AEr over 48 h after the last observation of the object. POP solutions for different number of observation arcs are represented. Each curve represents the average value of the error over 17 GPS satellite solutions. Hashed grey bands represent potential future observation nights.

being close to 12 h. The initial guess is determined from a Gooding initial orbit determination[12], while the DSRA dynamical parameter is still initialized with $90\,\mathrm{nm\,s^{-2}}$. After the POD process, a mean value of $a_{\mathrm{IAM}} = 99.5\,\mathrm{nm\,s^{-2}}$ is obtained, with a standard deviation of $9.7\,\mathrm{nm\,s^{-2}}$, which is consistent with the values reported in Tab. 2 for GNSS satellites.

Fig. 6 plots the norm of the position error as a function of the number of orbital revolutions of each RSO, where curves represent the mean over the 17 GPS satellites and vertical bars represent the epochs of arc observations. Using

DOI: 10.13009/EUCASS2025-644

only gravitational models in the dynamics, we can expect inaccuracies to grow with time, thus PODs over a larger period will drastically increase the error over that entire period. This is confirmed by Fig. 6(a), where the best RMSEr over the whole period is near 30 m for 1 observation arc, and reaching almost 200 m when using 5 whole arcs of observation. On the contrary, Fig. 6(b) shows that adding the DSRA to the dynamics (and inferring the IAM dynamical parameter) causes a decrease in the RMSEr over time when the time window increases, starting at 64 m for 1 arc and reaching 14 m for 4 and 5 arcs.

Although CICLOPE should be able to detect DSRA-induced displacements, mismodeling effects, such as the assumption of a spherical RSO with isotropic absorbance or imperfect attitude control, become overly prominent and cannot be averaged out over a single arc. A larger time window thus allows for a more reliable IAM dynamical parameter inference. However, we can also note that having more than 4 consecutive arcs does not increase the RMSEr value of the POD. A rather curious observation is about the shapes of the curves. Using solely gravitational models gives a POD with the best estimation at the middle epoch of the observations and a decreasing accuracy away from it. Oppositely, adding the DSRA in the dynamics generates a slightly better estimation near the edges, even though peaks remains constant.

Fig. 7 shows the same quantities but predicted after the last observation of the RSO, to evaluate the quality of the POP. Here, the hashed vertical bars represent the future nights of potential observations. We can draw the same conclusions for Fig. 7(a) than for the POD. However, using a single measurement arc, the error increases drastically over time, meaning that the initial state is under-constrained, as for Fig. 7(b), where we see that the addition of a misestimated parameter leads to an even worst solution. With 2 observed arcs, the state inference is better, although increasing furthermore the number of arcs decreases the accuracy on both plots. This effect is exacerbated in the case of DSRA modeling: having more arcs allows a better estimation of the IAM dynamical parameter, however, the error due to the mismodelings of the model slowly accumulates with time (and thus with the increased number of arcs of observation), hindering the accuracy of the POP. Therefore, using the IAM, the best POP can be obtained with 2 to 3 arcs of observation with a 30 m accuracy over a 48 h horizon. This suggests that a sequential estimation of the RSO's state over a 2- to 3-day window provides improved accuracy while requiring fewer computational resources than a complete tracking over longer time spans.

4.4 Validation with experimental optical measurements

The final step of our approach is to validate the measurement chain through a complete POD and POP process. Data were acquired over two consecutive nights with our PGBOS CICLOPE. The target was NAVSTAR82 (NORAD ID: 55268), observed on September 8th (for 2 h) and September 9th (for 4 h), 2023. It has a revolution period of about 11 h 57 min, and is on a low eccentricity (3×10^{-4}) orbit with a 55° inclination. With a sampling of about 3 observations per hour, we were able to perform a POD and a POP of the RSO. Fig. 8(a) and (b) plot the error components along 3 axis (radial, along-track, and cross-track) and the total error norm. We see that, using only gravitational model, the error of the estimation quickly increases after the last observation, reaching a hectometric positional error after 24 h, similar to the simulations. The estimation of the DSRA and its inclusion in the dynamics allows us to gain an order of magnitude of accuracy as demonstrated on simulated data, reaching a decametric accuracy up to 48 h after the last observation of the RSO.

Although the same reasoning applies to Fig. 8(a), let us focus on Fig. 8(b) where the effect appears more clearly. It reveals a periodic error pattern peaking on the opposite side of the orbit (i.e., half a revolution later). This is a direct consequence of ground-based observations, which roughly sample the same orbital arc each night. As a result, estimation accuracy degrades on the unobserved segments. Furthermore, the dominant error lies in the along-track direction. Starting from a minimum, the estimated solution lags behind the reference while its radial component, and thus its potential energy, is higher than that of the reference. Later, the opposite occurs: the estimate begins to catch up as its altitude (i.e., radial component) becomes lower than that of the reference. These periodic variations in velocity and altitude errors are commonly linked to inaccuracies in the estimated eccentricity. Additionally, in near-circular orbits, the orientation of the ellipse defined by the argument of perigee is difficult to estimate precisely. Since solar radiation pressure (SRP) is known to primarily affect eccentricity,[16] our POD likely remains sensitive to residual SRP mismodeling.

The angle-only nature of the observations primarily affects the radial component, and, as previously noted, also contributes to along-track error due to their correlation. This is mainly due to the observation geometry: the sensor is located on the Earth's surface, while the RSO orbits around the Earth's center, which limits direct sensitivity to the radial direction. However, the orbital period is well constrained by the sequence of observations acquired over two consecutive nights, allowing for an accurate estimation of the semi-major axis. For low-eccentricity orbits, this directly yields a reliable estimate of the radial position. As a result, radial error is not the main limiting factor in the current POD and POP performance.

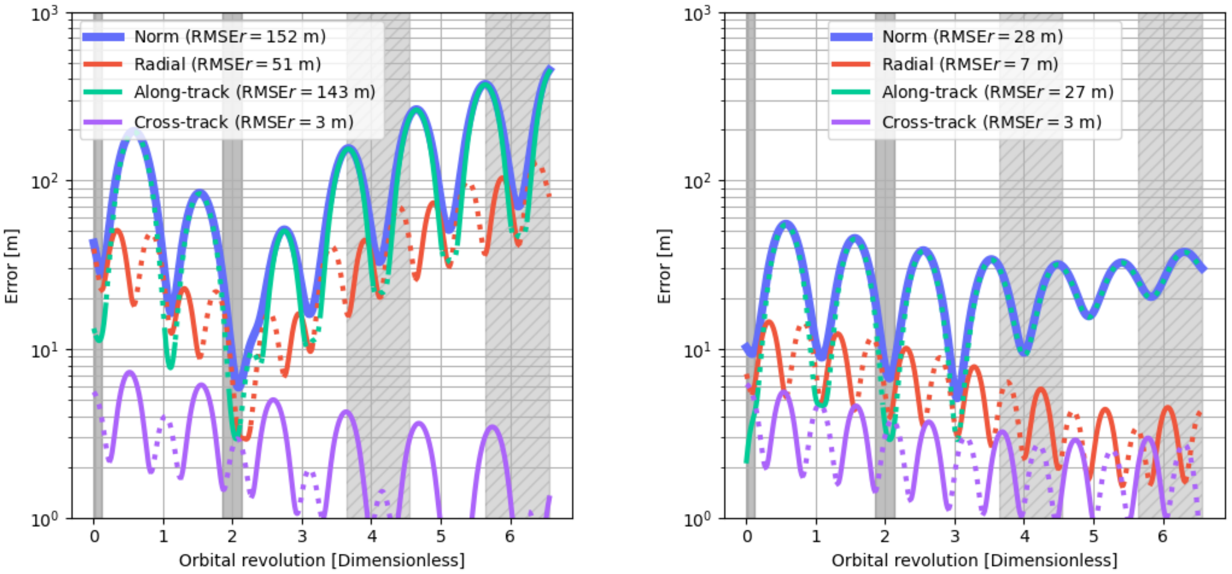

(a) Gravitational models only.

(b) Isotropic absorbance included.

Figure 8: POD and POP accuracy on the satellite NAVSTAR 82 observed the 8th and 9th of September 2023. Due to the logarithmic scale of the y-axis, we show absolute values of the errors. Dotted lines represent negative values. A Gaussian filter was applied to smooth the curves. Solid and hashed grey bands respectively represent past observations and potential future observation nights.

5. Conclusion

This paper demonstrates that a simple modeling approach, incorporating a few orders of the Earth geopotential, the Moon and Sun interactions, and an isotropic absorbance modeling of the DSRA, can accurately describe the orbit of a GNSS RSO over a 2-day horizon with decametric accuracy. Notably, this level of accuracy is within reach of modern PGBOS, which motivated the confrontation of POP methods to real angle-only data. This methodology involves estimating orbital parameters from accurate optical measurements on non-cooperative targets over at least two distinct observation arcs, and then propagating the estimated state over several days.

Our work confirms these predictions in two significant ways. By introducing representative detection noise into precise ephemeride data from GNSS satellites, simulating an optical station's angular measurements, we achieved an RMSEr of 22 m using only 2 observation arcs, and as low as 14 m with 4 consecutive arcs. Based on this POD, we successfully performed a POP with 30 m accuracy over a 48 h period.

Using our limited optical data available, we demonstrated for the first time, to the best of our knowledge, that PGBOSs allow for decametric accuracy POP, provided that measurement data exhibits a typical accuracy of 50 mas, observations span several consecutive nights, and the time window excludes potential maneuvers. This achievement paves the way for accurate management of congested MHOs, to prevent collisions and extend beyond immediate safety concerns. It also opens the door to more sophisticated SSA systems such as the imaging of GEO RSOs[14,23], since most of the error is along-track while the across-track error is only a few meters and the radial error is irrelevant.

6. Acknowledgments

This work has made use of data from the European Space Agency (ESA) mission *Gaia* (`https://www.cosmos.esa.int/gaia`), processed by the *Gaia* Data Processing and Analysis Consortium (DPAC, `https://www.cosmos.esa.int/web/gaia/dpac/consortium`). Funding for the DPAC has been provided by national institutions, in particular the institutions participating in the *Gaia* Multilateral Agreement. This work made use of Astropy[†]: a community-developed core Python package and an ecosystem of tools and resources for astronomy[2]. This work made use of Scipy[‡]: a Python-based ecosystem of software for mathematics, science, and engineering.[26] This research made use

---

[†] http://www.astropy.org

[‡] https://scipy.org/

DOI: 10.13009/EUCASS2025-644

of data provided by Astrometry.net. The authors thank Eric Glemet for the on-going automation of the CICLOPE telescope and Dominique Fressard for the work at Salon-de-Provence. This work is supported by PhD Grant DGA/AID 2024302.

References

[1] Mark R Ackermann, Pete Zimmer, John McGraw, and Eric Kopit. COTS options for low-cost SSA. Technical report, Sandia National Lab.(SNL-NM), Albuquerque, NM (United States), 2015.

[2] Astropy Collaboration. The Astropy Project: Sustaining and Growing a Community-oriented Open-source Project and the Latest Major Release (v5.0) of the Core Package. *Astrophys. J.*, 935(2):167, August 2022.

[3] Astropy Collaboration, A. M. Price-Whelan, B. M. Sipőcz, H. M. Günther, P. L. Lim, and S. M. et al. Crawford. The astropy project: Building an inclusive, open-science project and status of the v2.0 core package. *The Astronomical Journal*, 156(3):123, 2018.

[4] Astropy Collaboration, T. P. Robitaille, E. J. Tollerud, P. Greenfield, M. Droettboom, and E. et al. Bray. Astropy: A community python package for astronomy. *Astronomy & Astrophysics*, 558, 2013.

[5] Stéphane Basa et al. COLIBRI, a wide-field 1.3 m robotic telescope dedicated to the transient sky. In Heather K. Marshall, Jason Spyromilio, and Tomonori Usuda, editors, *Ground-based and Airborne Telescopes IX*, volume 12182, page 121821S. International Society for Optics and Photonics, SPIE, 2022.

[6] J. C. Bennett, Jizhang Sang, C. H. Smith, and K. Zhang. Accurate orbit predictions for debris orbit manoeuvre using ground-based lasers. *Advances in Space Research*, 52(11):1876–1887, 2013.

[7] Thomas Delaite. *Optical detection and localisation for space surveillance*. PhD thesis, Université Paris-Saclay, 2024.

[8] Thomas Delaite, Jocelyn Couetdic, Éric Glémet, and Frederic Cassaing. Performance of an Optical COTS Station for the wide-field Detection of Resident Space Objects. In *The Advanced Maui Optical and Space Surveillance Technologies (AMOS) Conference*, September 2023.

[9] J. R. Dormand and P. J. Prince. A family of embedded runge-kutta formulae. *Journal of Computational and Applied Mathematics*, 6(1):19–26, 1980.

[10] ESA Space Debris Office. Esa's space debris environment report – ninth edition. Technical Report ESA/SD/REP-09, European Space Agency (ESA), March 2025. Accessed: 2025-06-08.

[11] Gaia Collaboration. *Gaia* data release 3: Summary of the content and survey properties. *Astron. Astrophys.*, 674, June 2023.

[12] Robert H Gooding. A new procedure for the solution of the classical problem of minimal orbit determination from three lines of sight. *Celestial Mechanics and Dynamical Astronomy*, 66:387–423, 1996.

[13] Hanae Labriji, Olivier Herscovici-Schiller, and Fréderic Cassaing. Computation of the lateral shift due to atmospheric refraction. *Astronomy & Astrophysics*, 662:A61, 2022.

[14] Hanae Labriji, Olivier Herscovici-Schiller, and Frédéric Cassaing. Shadow imaging of geostationary satellites: experimental demonstration with accurate polychromatic modelling of diffraction and atmospheric disturbances. In *Advanced Maui Optical and Space Surveillance Technologies Conference (AMOS)*, 2022.

[15] E Lacruz, C Abad, JJ Downes, F Hernández-Pérez, D Casanova, and E Tresaco. High astrometric precision in the calculation of the coordinates of orbiters in the geo ring. *Revista mexicana de astronomía y astrofísica*, 54(1):0–0, 2018.

[16] J. C. Liou and J. K. Weaver. Orbital Dynamics of High Area-To Ratio Debris and Their Distribution in the Geosynchronous Region. In D. Danesy, editor, *Proceedings of the 4th European Conference on Space Debris*, volume 587 of *ESA Special Publication*, page 285, August 2005.

[17] Jared Maruskin. *Dynamical Systems and Geometric Mechanics: An Introduction*, volume 48. Walter de Gruyter GmbH & Co KG, 2018.

DOI: 10.13009/EUCASS2025-644

[18] Oliver Montenbruck and Eberhard Gill. *Satellite Orbits: Models, Methods and Applications*. Springer, Berlin, Heidelberg, 2000.

[19] Oliver Montenbruck, Peter Steigenberger, and Urs Hugentobler. Enhanced solar radiation pressure modeling for galileo satellites. *Journal of Geodesy*, 89:283–297, 2015.

[20] F.J. Montojo, T. López Moratalla, and C. Abad. Astrometric positioning and orbit determination of geostationary satellites. *Advances in Space Research*, 47(6):1043–1053, 2011.

[21] Nikolaos K. Pavlis, Simon A. Holmes, Steven C. Kenyon, and James K. Factor. The development and evaluation of the earth gravitational model 2008 (egm2008). *Journal of Geophysical Research: Solid Earth*, 117(B4):B04406, 2012.

[22] Justin Romberg. Stable reconstruction with the truncated svd. Lecture notes, Georgia Tech ECE 6250, 2016. Available at `https://www.cc.gatech.edu/~justin/6250/`, accessed June 2025.

[23] Douglas B Ruyle, David H Curtis, and Peter N Mcmahon-Crabtree. Investigation of varying telescope array spacing for shadow imaging reconstruction from partial diffraction patterns. *Applied Optics*, 64(18):E101–E118, 2025.

[24] Jizhang Sang and James C. Bennett. Achievable debris orbit prediction accuracy using laser ranging data from a single station. *Advances in Space Research*, 54(1):119–124, 2014.

[25] Jizhang Sang, Bin Li, Junyu Chen, Pin Zhang, and Jinsheng Ning. Analytical representations of precise orbit predictions for earth orbiting space objects. *Advances in Space Research*, 59(2):698–714, 2017.

[26] SciPy Community. SciPy: Open source scientific computing library. `https://scipy.org/`.

[27] Leonid Shakun et al. Comparison of the lemur and psst image processing pipelines for astrometric measurements of resident space objects in all orbital regimes. In *Advanced Maui Optical and Space Surveillance Technologies Conference (AMOS)*, 2023.

[28] L. F. Shampine. Some practical runge-kutta formulas. *Mathematics of Computation*, 46(173):135–150, 1986.

[29] Jovan Skuljan. High-precision astrometric measurements of calibration satellites. In *Advanced Maui Optical and Space Surveillance Technologies Conference*, 2022.

[30] Byron D. Tapley, Bob E. Schutz, and George H. Born. *Statistical Orbit Determination*. Elsevier Academic Press, Burlington, MA, 2004.

[31] CICLOPE team. Ciclope internal technical note, to be published.

[32] David A. Vallado. *Fundamentals of Astrodynamics and Applications*, volume 12 of *Space Technology Library*. Microcosm Press, Hawthorne, CA, 4 edition, 2013.

[33] Pauli Virtanen, Ralf Gommers, Travis E. Oliphant, Matt Haberland, Tyler Reddy, David Cournapeau, Evgeni Burovski, Pearu Peterson, Warren Weckesser, Jonathan Bright, Stéfan J. van der Walt, Matthew Brett, Joshua Wilson, K. Jarrod Millman, Nikolay Mayorov, Andrew R. J. Nelson, Eric Jones, Robert Kern, Eric Larson, C. J. Carey, İlhan Polat, Yu Feng, Eric W. Moore, Jake VanderPlas, Denis Laxalde, Josef Perktold, Robert Cimrman, Ian Henriksen, E. A. Quintero, Charles R. Harris, Anne M. Archibald, Antônio H. Ribeiro, Fabian Pedregosa, Paul van Mulbregt, and SciPy 1.0 Contributors. SciPy 1.0: Fundamental algorithms for scientific computing in python. *Nature Methods*, 17:261–272, 2020.

[34] Chengxing Zhai, Michael Shao, Navtej Saini, Philip Choi, Nez Evans, Russell Trahan, Kutay Nazli, and Max Zhan. Near-earth object observations using synthetic tracking. *Publications of the Astronomical Society of the Pacific*, 136(3):034401, mar 2024.

[35] Zheng-Hai Zhu, Jing-Hui Zheng, Hao Luo, Guo-Ping Chen, Wei Wang, Yin-Dun Mao, Wen-Tang Wu, and Kun-Peng Wang. CMOS-based observation of resident space objects using short-exposure stacking mode. *Advances in Space Research*, 72(6):2064–2077, 2023.